Monthly Notices
of the
ROYAL ASTRONOMICAL SOCIETY

Mon. Not. R. Astron. Soc. (2011) doi:10.1111/j.1365-2966.2011.18996.x

Solar-like oscillations from the depths of the red-giant star KIC 4351319 observed with *Kepler*

M. P. Di Mauro,[1⋆] D. Cardini,[1] G. Catanzaro,[2] R. Ventura,[2] C. Barban,[3] T. R. Bedding,[4] J. Christensen-Dalsgaard,[5] J. De Ridder,[6] S. Hekker,[7,8] D. Huber,[4] T. Kallinger,[9,10] A. Miglio,[7,11] J. Montalban,[11] B. Mosser,[3] D. Stello,[4] K. Uytterhoeven,[12,13] K. Kinemuchi,[14] H. Kjeldsen,[5] F. Mullally[15] and M. Still[14]

[1]*INAF – IASF, Istituto di Astrofisica Spaziale e Fisica Cosmica, Via del Fosso del Cavaliere 100, 00133 Roma, Italy*
[2]*INAF – Osservatorio Astrofisico di Catania, Via S. Sofia 78, 95123 Catania, Italy*
[3]*LESIA, CNRS, Université Pierre et Marie Curie, Université Denis, Diderot, Observatoire de Paris, 92195 Meudon Cedex, France*
[4]*Sydney Institute for Astronomy (SIfA), School of Physics, University of Sydney, NSW 2006, Australia*
[5]*Institut for Fysik og Astronomi, Bygn. 1520, Aarhus Universitet, Ny Munkegade, DK-8000 Aarhus C, Denmark*
[6]*Institut voor Sterrenkunde, K. U. Leuven, Celestijnenlaan 200D, 3001 Leuven, Belgium*
[7]*School of Physics and Astronomy, University of Birmingham, Birmingham B15 2TT*
[8]*Astronomical Institute 'Anton Pannekoek', University of Amsterdam, Science Park 904, 1098 XH Amsterdam, the Netherlands*
[9]*Department of Physics and Astronomy, University of British Columbia, Vancouver, Canada*
[10]*Institute of Astronomy, University of Vienna, 1180 Vienna, Austria*
[11]*Institut d'Astrophysique et de Géofisique de l'Universitè de Liège, Allè du 6 Aout 17-B 4000 Liège, Belgium*
[12]*Laboratoire AIM, CEA/DSM-CNRS-Université Paris Diderot, CEA, IRFU, SAp, Centre de Saclay, 91191 Gif-sur-Yvette, France*
[13]*Kiepenheuer-Institut für Sonnenphysik, Schöneckstraße 6, 79104 Freiburg im Breisgau, Germany*
[14]*Bay Area Environmental Research Institute/NASA Ames Research Center, Moffett Field, CA 94035, USA*
[15]*SETI Institute/NASA Ames Research Center, Moffett Field, CA 94035, USA*

Accepted 2011 May 2. Received 2011 May 2; in original form 2011 January 10

ABSTRACT

We present the results of the asteroseismic analysis of the red-giant star KIC 4351319 (TYC 3124-914-1), observed for 30 d in short-cadence mode with the *Kepler* satellite. The analysis has allowed us to determine the large and small frequency separations, $\Delta\nu_0 = 24.6 \pm 0.2\,\mu$Hz and $\delta\nu_{02} = 2.2 \pm 0.3\,\mu$Hz, respectively, and the frequency of maximum oscillation power, $\nu_{\rm max} = 386.5 \pm 4.0\,\mu$Hz.

The high signal-to-noise ratio of the observations allowed us to identify 25 independent pulsation modes whose frequencies range approximately from 300 to 500 μHz.

The observed oscillation frequencies together with the accurate determination of the atmospheric parameters (effective temperature, gravity and metallicity), provided by additional ground-based spectroscopic observations, enabled us to theoretically interpret the observed oscillation spectrum.

KIC 4351319 appears to oscillate with a well-defined solar-type p-mode pattern due to radial acoustic modes and non-radial nearly pure p modes. In addition, several non-radial mixed modes have been identified.

Theoretical models well reproduce the observed oscillation frequencies and indicate that this star, located at the base of the ascending red-giant branch, is in the hydrogen-shell-burning phase, with a mass of $\sim$1.3 $M_\odot$, a radius of $\sim$3.4 $R_\odot$ and an age of $\sim$5.6 Gyr. The main parameters of this star have been determined with an unprecedented level of precision for a red-giant star, with uncertainties of 2 per cent for mass, 7 per cent for age, 1 per cent for radius and 4 per cent for luminosity.

Key words: stars: AGB and post-AGB – stars: evolution – stars: fundamental parameters – stars: individual: KIC 4351319 – stars: oscillations – stars: solar-type.

⋆E-mail: mariapia.dimauro@iasf-roma.inaf.it

1 INTRODUCTION

Oscillations excited by turbulent convection – solar-like oscillations – have been successfully identified in cool main-sequence and post-main-sequence stars with convective envelopes. In the red giants, solar-like oscillations have been first detected by ground-based observations (Merline 1999; Frandsen et al. 2002; Stello et al. 2004) and by the *Wide Field Infrared Explorer* (*WIRE*) satellite (Buzasi et al. 2000; Retter et al. 2003, 2004).

Difficulties in the identification of the observed modes led several authors (Guenther, Demarque & Buzasi 2000; Dziembowski et al. 2001; Teixeira et al. 2003; Christensen-Dalsgaard 2004) to speculate on the pulsational properties of the red-giant stars. Red giants are characterized by a deep convective envelope and a small degenerate helium core. Since the density in the core of these stars is quite large, the buoyancy frequency can reach very large values in the central part. In these conditions, g modes of high frequencies can propagate and might eventually interact with p modes giving rise to modes of mixed character. As a consequence, the spectrum of the red giants is predicted to have a quite complicated appearance, with a sequence of peaks uniformly spaced in frequency due to acoustic modes, and other peaks with less clear pattern due to mixed modes.

The detection of solar-like oscillations in red giants has been well established by the space mission *Microvariability & Oscillations of Stars* (*MOST*) (Barban et al. 2007; Kallinger et al. 2008a,b), while the *Convection Rotation and Planetary Transit* (*CoRoT*) satellite was able to detect for the first time non-radial modes in red-giant stars (De Ridder et al. 2009) and to find solar-like oscillations in a very large sample of G and K giant stars (Hekker et al. 2009; Kallinger et al. 2010a; Mosser et al. 2010) mainly lying in the core-helium-burning evolutionary phase (Miglio et al. 2009).

The high-quality observations of the *Kepler* mission (Borucki et al. 2010; Koch et al. 2010) enabled to extend the detection of solar-like oscillations from the red clump to the lower luminosity region of the red-giant branch (Bedding et al. 2010; Hekker et al. 2010b; Huber et al. 2010; Kallinger et al. 2010b), where stars are still burning H in the shell. This finding enables us to study the structure and the evolution of the stars from the main-sequence phase up to advanced evolutionary stages by means of asteroseismology (Gilliland et al. 2010).

In this article we present the results of the analysis of the oscillation spectrum of the red giant KIC 4351319 (TYC 3124-914-1, ESA 1997) – nicknamed 'Pooh' (Milne 1926) within the authorship team – observed by the *Kepler* satellite for 30 d in short-cadence mode (integration time ∼1 min; Gilliland et al. 2010). Here, we also consider the theoretical interpretation of the observations and derive the asteroseismic estimates of age, mass and radius and of other structural characteristics, making use of the accurate atmospheric parameters obtained by ground-based spectroscopy performed at McDonald Observatory.

The star selected for this study is of particular interest because its oscillation spectrum shows an excess of power centred at frequency ∼380 μHz, higher than is typical for *Kepler* red giants (Bedding et al. 2010; Hekker et al. 2010b; Huber et al. 2010; Kallinger et al. 2010b). This indicates that the star is well below the red clump in luminosity and is still ascending the red-giant branch (Miglio et al. 2009). Its relatively high frequencies require *Kepler*'s short-cadence mode (see Section 4), which means that only relatively few stars with these characteristics are being observed by *Kepler*. KIC 4351319 therefore provides a very important opportunity to study this evolutionary phase and hence it has been selected for long-term observations by *Kepler*.

2 ATMOSPHERIC PARAMETERS FROM SPECTROSCOPY

Spectroscopic observations of KIC 4351319 in the visible spectral range have been carried out on 2010 July 26 (HJD = 245 5404.7756) with the Cross-Dispersed Echelle Spectrograph at the 2.7-m 'Harlan J. Smith' telescope at the McDonald Observatory, Texas, USA, in the framework of the ground-based observational support of the *Kepler* space mission (Uytterhoeven et al. 2010a,b).

A stellar spectrum, wavelength-calibrated and normalized to the continuum, was obtained using standard data-reduction procedures for spectroscopic observations within the NOAO/IRAF package. The resulting signal-to-noise ratio (S/N) was S/N ≈ 100. The spectral resolution as measured from the Th–Ar emission lines is about $R = 65\,000$.

In order to derive the effective temperature and surface gravity for our target, we minimized the difference between observed and synthetic profiles. As a goodness-of-fit test we used the parameter:

$$\chi^2 = \frac{1}{N} \sum \left(\frac{I_{\rm obs} - I_{\rm th}}{\delta I_{\rm obs}} \right)^2 ,$$

where N is the total number of independent points in the spectrum, $I_{\rm obs}$ and $I_{\rm th}$ are the intensities of the observed and computed profiles, respectively, and $\delta I_{\rm obs}$ is the photon noise. The synthetic spectra were generated in three steps: first we computed the stellar atmosphere model by using the ATLAS9 code (Kurucz 1993), then the stellar spectrum was synthesized using SYNTHE (Kurucz & Avrett 1981) and finally the instrumental and rotational convolutions were applied. The ATLAS9 code includes the metal opacity by means of distribution functions (ODF) that are tabulated for multiples of the solar metallicity and for various microturbulence velocities.

We selected a set of vanadium and iron lines in the range between 6180 and 6280 Å, which are free of blending and whose atomic parameters are well known and already explored for temperature calibrations (see Biazzo et al. 2007, and reference therein). For surface gravity we used the non-saturated line Ca I at 6162.173 Å, whose wings are very sensitive to gravity changes (see Grey 1992).

First of all, we computed the $v \sin i$ of the star by using the parameters from the KIC catalogue (Latham et al. 2005) reported in Table 1. We used SYNTHE to reproduce the observed metal lines, and our best match was achieved convolving the computed lines with a stellar rotational profile having $v \sin i = 6 \pm 1\,{\rm km\,s^{-1}}$, while the microturbulent velocity $\xi = 1\,{\rm km\,s^{-1}}$ was obtained by using the relation $\xi = \xi(T_{\rm eff}, \log g)$ published by Allende Prieto et al. (2004). Then, with an iterative procedure starting with the values of the KIC catalogue of $T_{\rm eff}$ and $\log g$ and the solar abundances given by Asplund et al. (2009), we obtained the best-fitting values reported in Table 1. Uncertainties in $T_{\rm eff}$ and $\log g$ have been estimated

Table 1. Basic parameters of KIC 4351319.

	KIC and SIMBAD catalogues	Present analysis
V	10.19 [a]	–
$v \sin i$	–	$6 \pm 1\,{\rm km\,s^{-1}}$
$T_{\rm eff}$	$4725 \pm 200\,{\rm K}$ [b]	$4700 \pm 50\,{\rm K}$
$\log g$	3.353 ± 0.5 dex [b]	3.3 ± 0.1 dex
[Fe/H]	-0.563 ± 0.5 dex [b]	0.23 ± 0.15 dex

[a] http://simbad.u-strasbg.fr/simbad/ (CDS, Strasbourg, France)
[b] http://archive.stsci.edu/kepler/kepler_fov/search.php (Latham et al. 2005)

Table 2. Summary of the inferred abundances in the atmosphere of KIC 4351319.

El	$[X/H]$
Na	0.39 ± 0.15
Mg	-0.02 ± 0.14
Si	0.58 ± 0.09
Ca	0.10 ± 0.10
Sc	0.22 ± 0.14
Ti	0.09 ± 0.19
V	0.13 ± 0.14
Cr	0.39 ± 0.14
Mn	-0.01 ± 0.14
Fe	0.23 ± 0.15
Co	0.31 ± 0.12
Ni	0.26 ± 0.25
Zn	0.24 ± 0.16
Y	-0.18 ± 0.16
Zr	-0.18 ± 0.15
Ba	-0.06 ± 0.17
La	0.06 ± 0.15

within a 1σ level of confidence, as the variation in the parameters which increases the χ^2 by 1 (Lampton, Margon & Bowyer 1976). The uncertainty in the iron abundance is the standard deviation of the weighted average of the abundances derived from each single line. After having fixed $T_{\rm eff}$, $\log g$ and [Fe/H], we used SYNTHE to derive the abundance pattern of our target by the method of spectral synthesis. The results are summarized in Table 2 and plotted in Fig. 1. We then conclude that, according to estimated errors, the metallicity is slightly over the solar ones. In particular, iron abundance is equal to [Fe/H] $= 0.23 \pm 0.15$ dex.

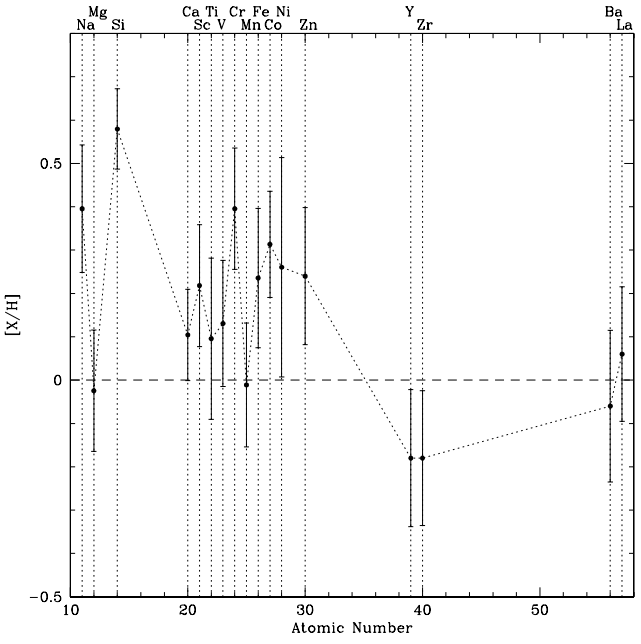

Figure 1. Abundance pattern computed for all metals detected in the spectrum recorded with the 'Harlan J. Smith' telescope at the McDonald Observatory. The horizontal dashed line represents the solar abundance as given in Asplund et al. (2009).

3 SOLAR-LIKE PROPERTIES IN RED-GIANT STARS

3.1 Large and small separations

It is well known that the properties of solar-like oscillations in main-sequence stars can be described by adopting the asymptotic development (Tassoul 1980), which predicts that the oscillation frequencies $\nu_{n,l}$ of acoustic modes, characterized by radial order n, and harmonic degree l, for $l \ll n$ should satisfy the following approximation:

$$\nu_{n,l} \sim \Delta\nu \left(n + \frac{l}{2} + \epsilon \right), \tag{1}$$

where ϵ is a function of frequency and depends on the properties of the surface layers and $\Delta\nu$, known as the large frequency separation, is the inverse of the sound traveltime across the stellar diameter and is proportional to the square root of the mean density.

Thus, the solar-like oscillation spectra should show a series of equally spaced peaks separated by $\Delta\nu$ between p modes of the same degree and adjacent n:

$$\Delta\nu \sim \Delta\nu_l = \nu_{n+1,l} - \nu_{n,l}. \tag{2}$$

In addition, the solar-like power spectra are characterized by another series of peaks, whose separation is $\delta\nu_{l,l+2}$, known as the small separation:

$$\delta\nu_{l,l+2} = \nu_{n,l} - \nu_{n-1,l+2}, \tag{3}$$

which is sensitive to the chemical composition gradient in the central regions of the star and hence to its evolutionary state.

The determination of the large and small frequency separations can provide asteroseismic inferences on the mass and the age of main-sequence and post-main-sequence solar-type stars, using the so-called seismic diagnostic CD diagram (Christensen-Dalsgaard 1988). However, these two seismic indicators alone do not represent an unambiguous diagnostic tool for more evolved stars, for which the relation between the small and large separation is almost linear (Bedding et al. 2010; Montalbán et al. 2010; Mosser et al. 2010). On the other hand, it has been demonstrated that the stellar mass and radius of a solar-like star can successfully be derived, within 7 and 3 per cent, respectively (e.g. Kallinger et al. 2010a), from measurements of the large separation and $\nu_{\rm max}$, the frequency at which the oscillation signal reaches a maximum, by using the scaling laws given by Kjeldsen & Bedding (1995) and Bedding & Kjeldsen (2003).

Hence, in order to characterize in details the structure of a red-giant star, it is necessary to consider individual frequencies of oscillation and other oscillation properties, as we will discuss in the following.

3.2 The potential of the mixed modes

The properties of solar-like oscillations are expected to change as the stellar structure evolves. According to equation (1) and considering that $\Delta\nu \propto R^{-3/2}$, oscillation frequencies of a given harmonic degree should decrease as the star evolves and the radius increases and should be almost uniformly spaced by $\Delta\nu$ at each stage of evolution. However, in subgiants and red giants the radial modes seem to follow equation (1) closely, but the frequencies of some non-radial modes appear to be shifted from the regular spacing due to the occurrence of the so-called 'avoided crossing' (Christensen-Dalsgaard 2004). As the star evolves away from the main sequence, the core contracts and the radius expands, causing an increase of the

local gravitational acceleration and of the gradients in the hydrogen abundance, and hence of the buoyancy frequency in the deep interior of the star. As a consequence g modes with high frequencies are allowed to propagate and can interact with p modes of similar frequency and same harmonic degree, giving rise to modes with mixed character, which behave as g modes in the interior and p modes in the outer envelope (Aizenman, Smeyers & Weigert 1977). The interaction can be explained as the coupling of two oscillators of similar frequencies. The effect of the coupling becomes much weaker for modes with higher harmonic degree, since in these cases the gravity waves are better trapped in the stellar interior and hence better separated from the region of propagation of the acoustic waves (Dziembowski et al. 2001; Christensen-Dalsgaard 2004; Dupret et al. 2009).

It has been found by Montalbán et al. (2010), and observationally demonstrated by Huber et al. (2010), that the scatter of $l = 1$ modes caused by 'avoided crossing' decreases as the star goes up to the red-giant branch: as the luminosity increases and the core becomes denser, the $l = 1$ acoustic modes are better trapped and the oscillation spectra become more regular. Once the star ignites He in the core, the core expands and the external convective zone becomes shallower which has the effect of increasing the probability of coupling between g and p modes again.

Very recently, Beck et al. (2011) have demonstrated that the quality of the *Kepler* observations gives the possibility to measure the period spacings of mixed modes with gravity-dominated character which, like pure gravity modes, penetrate deeply in the core allowing to study the density contrast between the core region and the convective envelope and, like p modes, have amplitude at the surface high enough to be observed. In particular, Bedding et al. (2011) found that measurements of the period spacings of the gravity-dominated mixed modes permit to distinguish between hydrogen- and helium-burning stages of evolution of the red giants.

The occurrence of mixed modes is then a strong indicator of the evolutionary state of a red-giant star and the fitting of the observed modes with those calculated by theoretical models can provide not only mass and radius but, with a good approximation, also an estimate of the age of the star.

3.3 Sharp features inside the star

Sharp variations localized at a certain acoustic depth in the structure of pulsating stars produce a distinctive quasi-periodic signal in the frequencies of oscillations. The characteristics of such a signal are related to the location and thermodynamic properties of the layer where the sharp variation occurs. Sources of sharp variations are, for example, the borders of convection zones and regions of rapid variation in the first adiabatic exponent $\Gamma_1 = (\partial \ln p/\partial \ln \rho)_{\rm ad}$, where the derivative corresponds to an adiabatic change, such as the one that occurs in the region of the second ionization of helium.

In the main-sequence stars the signals coming from different sharp features in the interior overlap generating a complex behaviour (Mazumdar & Antia 2001). In red giants, a recent study by Miglio et al. (2010) demonstrated that the oscillatory signal of the frequencies observed is directly related only to the second helium ionization zone.

Several attempts have been made in order to isolate the generated oscillatory components from the frequencies of oscillations or from linear combinations of them such as large separations and second differences. In principle, this approach can be applied to determine the properties of the base of the convective envelope (Monteiro, Christensen-Dalsgaard & Thompson 2000; Ballot, Turck-Chièze & García 2004) and in particular to infer the helium abundance in the stellar envelope (Lopes et al. 1997; Monteiro & Thompson 1998; Pérez Hernández & Christensen-Dalsgaard 1998; Miglio et al. 2003; Basu et al. 2004; Houdek & Gough 2007).

4 *KEPLER* OBSERVATIONS AND ANALYSIS OF THE OSCILLATION SPECTRUM

KIC 4351319 has been observed by the *Kepler* satellite (Koch et al. 2010) during the Q0, Q1 and Q2 runs in long-cadence mode (integration time of ∼30 min) and during the Q3 run in short-cadence mode (integration time of ∼1 min). The data that we describe here were obtained during 30 consecutive days, starting on 2009 September 18, which correspond to the first month of observing quarter 3 (Q3.1). The *Kepler* short-cadence observation mode corresponds to a Nyquist frequency of 8497 μHz. In the present analysis, we used the *SOC corrected* data obtained by the *Kepler* team after reducing and correcting the raw photometric data for slopes and discontinuities as described in Jenkins et al. (2010) and García et al. (2011). The effective duty cycle resulted to be ∼97 per cent and the spectral window does not show aliasing artefacts that could interfere with the identification of real frequencies.

The top panel of Fig. 2 shows the cleaned light curve normalized to the mean value.

The Fourier analysis of the data set has been performed by using the PERIOD04 package (Lenz & Breger 2005), which allows to extract the individual frequencies from large multiperiodic time series – also containing gaps – and can perform multiple-frequency least-squares fit of up to several hundred simultaneous sinusoidal components. The resulting power spectrum of KIC 4351319 shows a clear power excess in the frequency range 300–500 μHz with regularly spaced peaks (bottom panel of Fig. 2), while no relevant features appear between 550 μHz and the Nyquist limit. We have considered only peaks in the spectrum with an S/N in amplitude greater than 3.

In order to confirm the results obtained, the analysis of the spectrum was also independently performed by five additional teams which adopted the following methods.

(a) The power spectrum was smoothed with a Gaussian with a full width at half-maximum (FWHM) of 0.5 μHz and the frequencies of the peaks with S/N > 3 (in amplitude) were measured.

(b) Peak-bagging methods, substantially based on the fit of Lorentzian profiles to the power density spectrum, using:

(i) maximum likelihood estimators (MLE) (see Appendix A for details).

(ii) Bayesian Markov-Chain Monte Carlo (MCMC) (Gruberbauer et al. 2009) (see Appendix B for details).

(iii) Envelope autocorrelation function analysis (Mosser & Appourchaux 2009).

Table 3 reports the set of frequencies confirmed, within the errors, by at least two of the peak-bagging solutions. Frequencies labelled with (•) have been detected by all the teams.

The values of the radial order for $l = 0$ are $n = 12$–18 as obtained by adopting the scaling law proposed by Mosser et al. (2011a) (see also Huber et al. 2010).

Three possible excited modes with $2 \leq$ S/N ≤ 3, namely 302.32 μHz, 387.12 μHz and 407.41 μHz, have been also found, but their validity must be carefully checked by additional future observations.

In order to estimate the large frequency separation, we first computed the autocorrelation function of the power spectrum in the

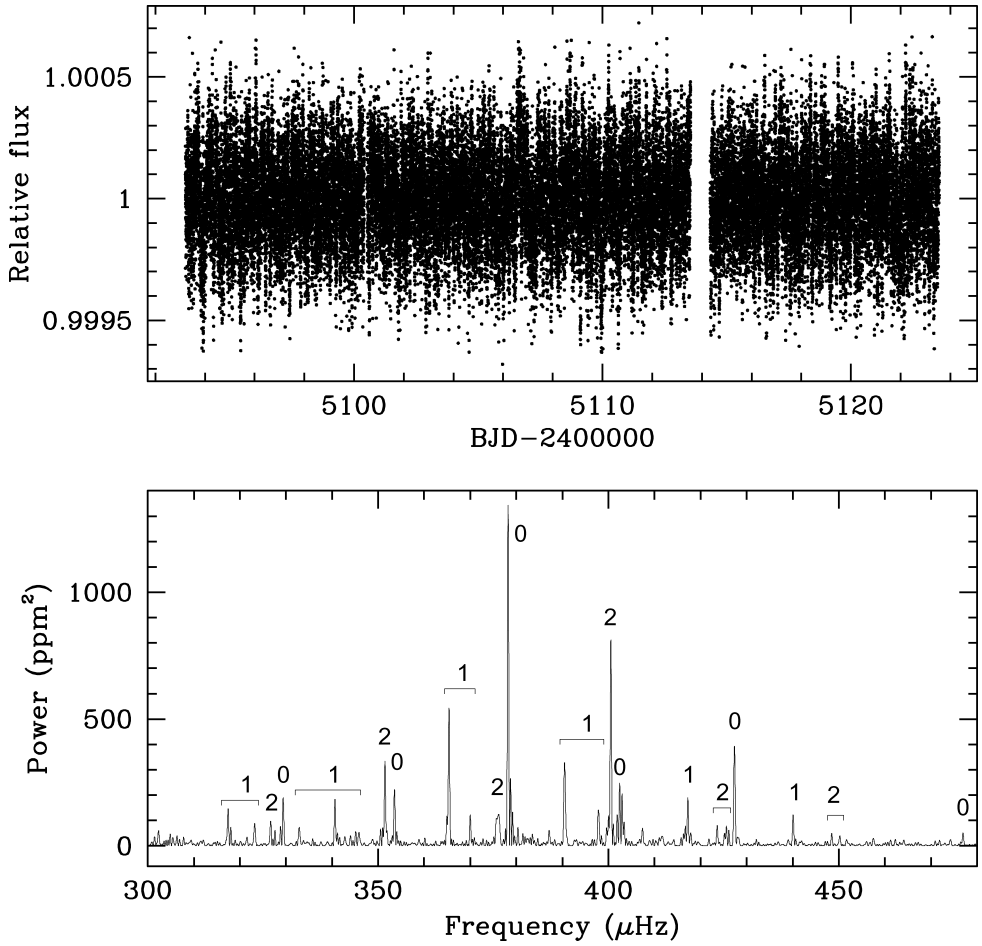

Figure 2. Top panel: light curve corrected for slopes and discontinuities and normalized to the mean value. Bottom panel: Fourier spectrum in the region of p-mode excess bump; harmonic degree of the excited modes is also shown.

region of p-mode power excess. With such an initial guess value of the large separation, we built an échelle diagram and identified the $l = 0$ ridge. Afterwards, we computed the comb-response function, as defined by Kjeldsen et al. (1995), for each frequency reported in Table 3 and for the three additional frequencies with $2 \leq \mathrm{S/N} \leq 3$, searching for the maximum value of the comb response in the range (15–30) μHz. The result, reported in Fig. 3, shows that many modes lie around the mean value of $\langle \Delta\nu_0 \rangle = 24.6 \pm 0.2$ μHz computed for the radial modes, while the other frequencies show a quite large scatter indicative of their mixed mode character.

Fig. 4 shows the region from 250 to 650 μHz of the power spectrum folded with a spacing equal to the mean value of the large frequency separation. Two sharp peaks, corresponding to modes with $l = 0$ and $l = 2$, as well as a broader peak, corresponding to modes with $l = 1$, can be clearly seen. The final mode identification in terms of the degree l, based on both the alignment in the échelle diagram (see Fig. 13) and the result of the peak bagging, is reported in Table 3. A value of the mean small frequency separation $\langle \delta\nu_{02} \rangle = 2.2 \pm 0.3$ μHz has been also derived from each pairs of $\nu_{n,0}$ and $\nu_{n-1,2}$ reported in Table 3.

4.1 Background and p-mode power excess modelling

After converting the power spectrum (ppm^2) to power spectral density (ppm^2 μHz^{-1}), by multiplying the power by the effective length of the observing run – estimated as the reciprocal of the area under the spectral window (Bedding et al. 2005) – a model fitting of the stellar background due to stellar activity and granulation has been performed. In order to simultaneously model the stellar background as well as the p-mode power excess, we fitted the observed power density spectrum by a superposition of white noise, two semi-Lorentzian functions (Harvey 1985) and a Gaussian function representing the power excess hump (see Kallinger et al. 2010a, for details):

$$P(\nu) = \sum_{i=1}^{2} \frac{A_i}{(1 + \nu B_i)^{c_i}} + D\mathrm{e}^{-\frac{(\nu_{\max} - \nu)^2}{2\sigma^2}} + E, \quad (4)$$

where ν is the frequency, A_i, B_i and c_i are the amplitudes, the characteristic time-scales and the slopes of the power laws; E is the white noise contribution; D, $\nu_{\max}$ and σ are the height, the central frequency and the width of the power excess hump, respectively.

We adopted as initial guess for the white noise the average of the power spectrum in the frequency range 1000–2000 μHz, where the photon noise is expected to dominate over the other components. The guess values for the remaining parameters have been evaluated by scaling from typical solar values (Aigrain, Favata & Gilmore 2004; Pallè et al. 1999; Huber et al. 2009) for active region and granulation time-scales. We smoothed the raw power spectrum density by applying a 4 μHz boxcar using the independent averages only, as suggested by García et al. (2009), in order to perform properly the fit by means of a weighted least-squares procedure. The weights we adopted, as in García et al. (2009), have been determined by

Table 3. KIC 4351319: observed oscillation frequencies with errors, their S/N and harmonic degree. The symbol • denotes modes confirmed by all the teams.

Freq (μHz)	S/N	l
329.16 ± 0.24	5.4	0
353.62 ± 0.20 •	5.4	0
378.34 ± 0.11 •	13.1	0
402.43 ± 0.07 •	5.5	0
427.32 ± 0.12 •	7.5	0
476.86 ± 0.54	3.6	0
317.38 ± 0.19 •	4.1	1
323.00 ± 0.20	3.4	1
332.98 ± 0.30	3.2	1
340.67 ± 0.09 •	5.6	1
345.26 ± 0.66	3.2	1
365.40 ± 0.07 •	8.9	1
370.09 ± 0.15	3.5	1
390.50 ± 0.09 •	6.1	1
397.89 ± 0.20	3.8	1
417.30 ± 0.11 •	5.1	1
440.20 ± 0.10 •	4.7	1
326.55 ± 0.25	4.0	2
351.32 ± 0.15 •	7.2	2
376.03 ± 0.19 •	5.0	2
400.56 ± 0.08 •	9.4	2
423.71 ± 0.40	3.4	2
425.80 ± 0.32 •	3.2	2
448.65 ± 0.40	3.4	2
449.98 ± 0.50	3.1	2

the uncertainties on each independent 4 μHz average. As in Mathur et al. (2010) we adopted the IDL least-squares MPFIT package (provided by Craig B. Markwardt, NASA/GSFC[1]), implementation of the Levenberg–Marquardt fitting algorithm. The results are shown in Fig. 5.

The fit returned, among other parameters, the maximum amplitude of the smoothed excess power $P_{\rm max} = 94.99 \pm 0.3$ ppm^2 μHz^{-1}. The corresponding frequency is $\nu_{\rm max} = 386.5 \pm 4.0$ μHz, where the uncertainty is given by the resolution of the smoothed spectrum. This value and its uncertainty are in a very good agreement with that found by fitting the raw spectrum by the envelope autocorrelation function analysis (Mosser & Appourchaux 2009).

Following Kjeldsen et al. (2008a), we evaluated the maximum amplitude per radial mode by adopting the calibration factor $c = 3.16$, whose value depends on the spatial response of the observations to modes with different degree relative to radial modes, and obtained $A_{\rm max} \simeq (27.19 \pm 0.16)$ ppm.

4.2 Global asteroseismic parameters

In order to extract a rough estimate of the global parameters of the star, to be adopted as guess values for the model computation, we adopted the scaling laws provided by Kjeldsen & Bedding (1995) and Bedding & Kjeldsen (2003), relating the observed mean large frequency separation 24.6 ± 0.2 μHz and $\nu_{\rm max} = 386.5 \pm 4.0$ μHz to the fundamental parameters of the star. We obtained: $M/{\rm M}_\odot \simeq 1.35 \pm 0.09$ and $R/{\rm R}_\odot \simeq 3.44 \pm 0.08$. We also derived the expected radial order of the mode with maximum amplitude in the spectrum, $n_{\rm max} \simeq 14$. This latter value is in agreement with the radial order identification of the radial mode with higher S/N reported in Section 4.

[1] http://cow.physics.wisc.edu/~craigm/idl/idl.html

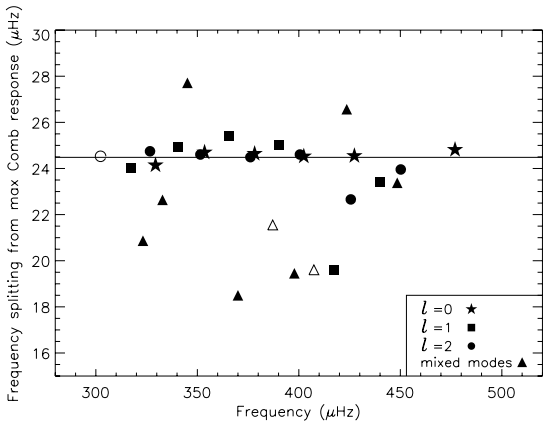

Figure 3. Large frequency separation as determined from the comb-response analysis applied to the frequencies of Table 3 (filled symbols) and to three possible frequencies with $2 \leq$ S/N ≤ 3 (open symbols). The horizontal line shows the mean value of 24.6 ± 0.2 μHz computed for the $l = 0$ modes of Table 3 only. The reported uncertainty is the standard deviation of the mean. Different symbols refer to $l = 0$ (stars), $l = 1$ (squares) and $l = 2$ (circles) modes, respectively, as derived by the alignment in the échelle diagram. Triangles refer to mixed modes (see text for more details).

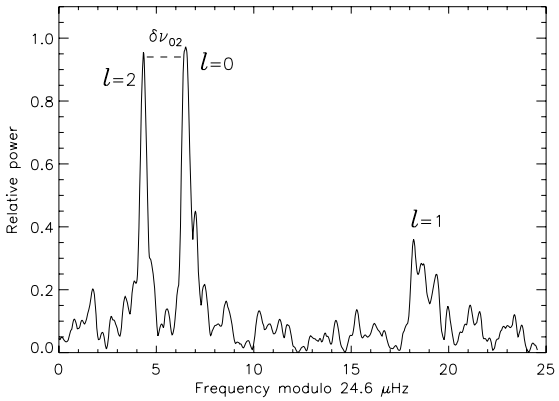

Figure 4. The power spectrum of KIC 4351319 folded at the average large separation, showing clear peaks corresponding to $l = 0$, 1 and 2. The small frequency separation $\delta\nu_{02}$ is also shown.

5 ON THE CHARACTERIZATION OF THE STRUCTURE OF KIC 4351319

5.1 Evolutionary models

Given the identified pulsation frequencies and the basic photospheric parameters, we faced the theoretical challenge to interpret the observed oscillation modes by constructing stellar models which satisfy the observational constraints.

We assumed the effective temperature and gravity as calculated in Section 2, respectively, $T_{\rm eff} = 4700 \pm 50$ K, $\log g = 3.3 \pm 0.1$ dex (Table 1).

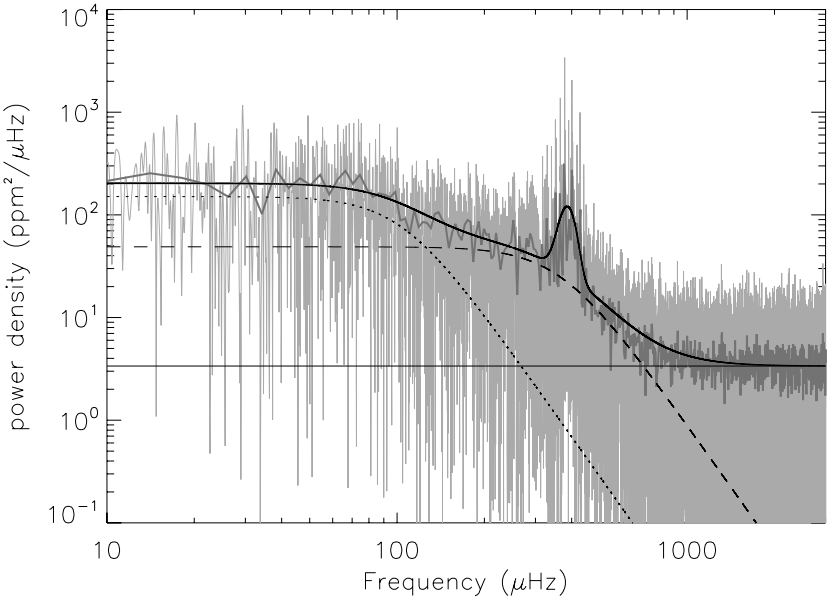

Figure 5. Power density spectrum of KIC 4351319. Light grey: power density spectrum; dark grey: the raw spectrum smoothed with a 4 μHz boxcar taking only the independent averages; thick solid line: global fit according to the model described in the text; dashed, dotted and dash–dotted lines: the two semi-Loretzians and the white noise component of the global fit, respectively.

We calculated several grids of theoretical structure models for the star by using the ASTEC evolution code (Christensen-Dalsgaard 2008a) by varying the mass and the composition in order to match the atmospheric parameters available.

All the models have been calculated with the OPAL2005 equation of state (Rogers & Nayvonov 2002), Opacity Project at Livermore (OPAL) opacities (Iglesias & Rogers 1996) and the Nuclear Astrophysics Compilation of Reaction rates (NACRE) nuclear reaction rates (Angulo et al. 1999). Convection was treated according to the mixing-length formalism (MLT) (Böhm-Vitense 1958) and defined through the parameter $\alpha = \ell/H_{\rm p}$, where $H_{\rm p}$ is the pressure scaleheight and α is assumed to vary from 1.6 to 1.8.

Inclusion of overshooting or diffusion outside the convective core during the main-sequence phase did not produce any appreciable effect on the oscillation frequencies of models in such evolved phases of the evolution.

A crucial input quantity is the iron abundance, whose logarithmic value relative to the solar one has been taken as [Fe/H] = (0.23 ± 0.15) dex, as determined in Section 2. The initial heavy element mass fraction Z can be calculated from the relation $[{\rm Fe/H}] = \log(Z/X) - \log(Z/X)_\odot$, where (Z/X) is the ratio at the stellar surface and the solar value is $(Z/X)_\odot = 0.0245$ (Grevesse & Noels 1993). Thus, it has been assumed that $Z/X = 0.04 \pm 0.01$. In the present modelling we neglect the difference in the relative abundances of the heavy elements between the star and the Sun (cf. Fig. 1); although this should be taken into account in future, more detailed investigations, the effects on the opacity and hence the model structure are likely to be contained within the assumed range of uncertainty in Z. The uncertainty in the observed value of Z introduces an uncertainty in the determination of the mass whose value, considering only the observed spectroscopic parameters, seems to be limited to the range $M = (0.8\text{–}1.5)\,{\rm M}_\odot$.

Extra mixing outside the convective region was obtained by adding turbulent diffusion from the convective envelope, as described in Proffitt & Michaud (1991), by using the parametrized formulation:

$$D = D_{\rm max}(\rho/\rho_{\rm b_{cz}})^{-3} \qquad (5)$$

where $\rho_{\rm b_{cz}}$ is the density at the base of the convective envelope and $D_{\rm max}$ is a parameter which sets the maximum diffusion.

Additional evolutionary models were calculated by including overshoot beneath the convective envelope by a distance $\ell_{\rm ov} = \alpha_{\rm ov} H_{\rm p,b_{cz}}$, where $H_{\rm p,b_{cz}}$ is the pressure scaleheight at the base of the convective envelope and $\alpha_{\rm ov}$ is a non-dimensional parameter.

The resulting evolutionary tracks are characterized by the mass M, the initial chemical composition and a mixing-length parameter. Fig. 6 shows a series of evolutionary tracks obtained for different masses and fixed initial composition and plotted in two Hertzsprung–Russell (HR) diagrams, representing respectively the effective temperature-gravity plane and the effective temperature-luminosity plane.

The location of the star in the HR diagram identifies KIC 4351319 as being in the post-main-sequence phase of evolution at the beginning of the ascending red-giant branch. It has a small, degenerate helium core, having exhausted its central hydrogen, and it is in the shell-hydrogen-burning phase, with a very deep convective zone, extending from the base located at about $r_{\rm b_{cz}} \simeq 0.2R$ to the photosphere.

Fig. 7 shows the internal content of hydrogen in three models of this star, which include respectively extra mixing by turbulent diffusion from the convective envelope, overshooting from the convective envelope with $\alpha_{\rm ov} = 0.2$ and without any extra mixing effect. The internal hydrogen profiles show that the core, where the hydrogen is exhausted, is very small and a sharp variation, as a step-like function, occurs at the base of the convective envelope located at $m_{\rm b_{cz}} = 0.28M$ and $r_{\rm b_{cz}} = 0.23R$ for the model with no extra effects considered. Models with inclusion of turbulent diffusion show a smooth profile of the abundance of the hydrogen with no sharp variation at the base of the envelope.

We expect to be able to distinguish among the different internal characteristics of the structure by studying the oscillation properties of this star. Furthermore, we wish to verify whether, as demonstrated by Christensen-Dalsgaard, Proffitt & Thompson (1993) for the case of the Sun, the inclusion of diffusion in the models results in a better agreement between theory and observations.

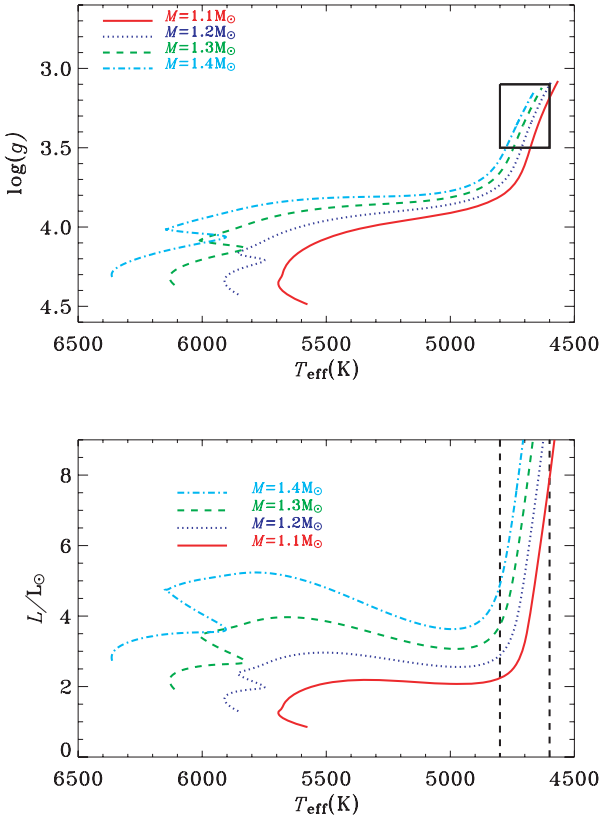

Figure 6. Evolutionary tracks plotted in the HR diagrams (the upper panel shows $T_{\rm eff} - \log g$, the lower panel shows $T_{\rm eff} - L$) calculated for increasing values of the mass, while all the other parameters are fixed. The metallicity is $Z = 0.03$, the initial hydrogen abundance $X_0 = 0.7$ and $\alpha = 1.8$. Here, no additional effects are included. The rectangle defines the 2σ error box for the observed gravity and effective temperature. In the bottom panel, black dashed lines indicate the uncertainty in the observed effective temperature while observed values of luminosity are not known.

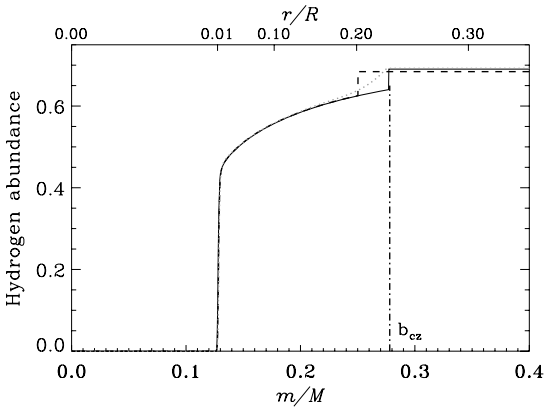

Figure 7. Hydrogen content in three models of KIC 4351319 computed with $M = 1.32\,{\rm M}_{\odot}$, $X_0 = 0.7$, $Z_0 = 0.03$, $\alpha = 1.8$. The base of the convective envelope located at $m_{\rm b_{cz}} = 0.28M$ and $r_{\rm b_{cz}} = 0.23R$ is shown by the dot–dashed line. The solid line corresponds to Model 1 in Table 4 with no additional effects. Dotted line corresponds to Model 3 calculated with inclusion of strong turbulent diffusion ($D_{\rm max} = 40000\,{\rm cm^2\,s^{-1}}$). Dashed line corresponds to Model 4 of Table 4 calculated with overshooting from the convective envelope.

5.2 The seismic properties of the models

In order to investigate the observed solar-like oscillations, we used the ADIPLS package (Christensen-Dalsgaard 2008b) to compute adiabatic oscillation frequencies with degree $l = 0$, 1, 2, 3 for all the models satisfying the spectroscopic constraints.

Fig. 8 shows the evolution of frequencies computed for an evolutionary model of KIC 4351319 calculated with $M = 1.32\,{\rm M}_{\odot}$, $Z = 0.03$, without additional extra mixing effects. The ranges in frequency and effective temperature have been chosen to correspond approximately to the observed ranges. The location of the acoustical cut-off frequency, decreasing with increasing age, at the top of the atmosphere in the model has been indicated by grey dots.

As it has been already explained in Section 3, according to equation (1) the plot should be characterized by frequencies which decrease as the star evolves and almost uniformly spaced by $\Delta\nu$ at each stage of evolution. In the case of more evolved stars, as it has been shown by Di Mauro et al. (2003) and Metcalfe et al. (2010), while the radial modes seem to follow closely equation (1), the frequencies of the modes with $l = 1$ show the typical oscillating behaviour due to the presence of the mixed modes. In addition, Fig. 8 shows that at each stage of the evolution the distance between two frequencies of adjacent orders becomes smaller and smaller as the frequency decreases: while the upper part of the panel hosts mixed modes with prevalent p-mode character, below 350 μHz the panel appears more crowded by mixed modes with predominant g-mode character and the general trend of frequencies decreasing as the star evolves no longer holds.

In particular, pure g modes of high radial order are located at very low frequencies and high radial orders, below 300 μHz.

Fig. 9 shows the evolution of the frequencies for $l = 2$ modes as a function of the age and the effective temperature. It shows that $l = 2$ modes, similarly to what happen for $l = 1$ modes, undergo avoided crossings during the evolution and the theoretical oscillation spectrum is as a result very crowded. The presence of mixed modes with the prevalent g-mode character is also evident for $l = 2$: below 400 μHz frequencies do not appear to decrease with the decrease of the effective temperature.

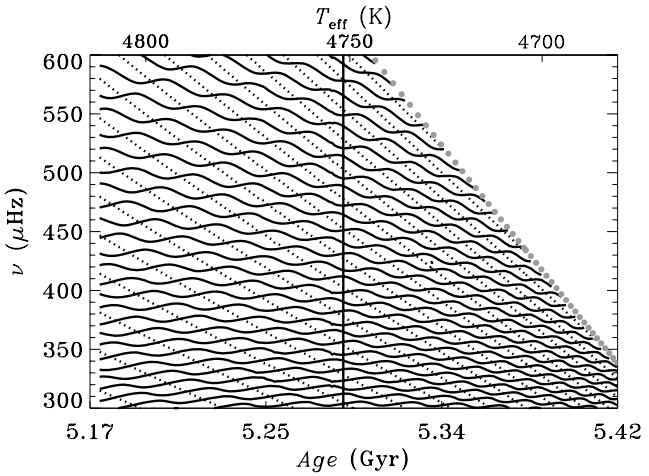

Figure 8. Evolution of adiabatic frequencies with age and with effective temperature of a model computed with a mass $M = 1.32\,{\rm M}_{\odot}$ and $Z = 0.03$. The dotted lines correspond to modes of degree $l = 0$, and the solid lines to modes with $l = 1$. The frequency and effective temperature ranges correspond to the observed ones. The grey dots indicate the acoustical cut-off frequency. The vertical line indicates Model 1 of Table 4.

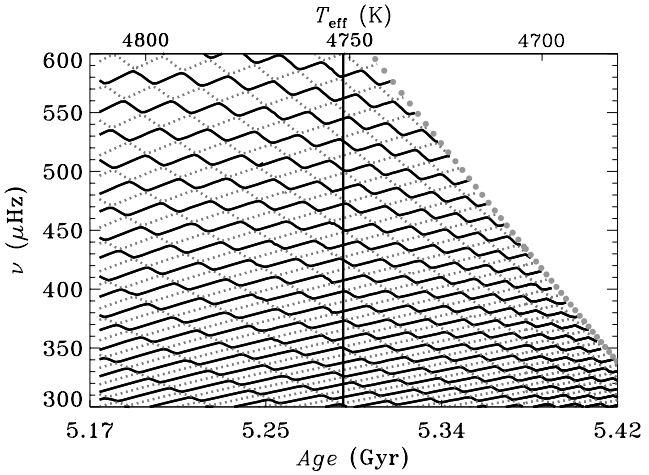

Figure 9. Evolution of adiabatic frequencies for modes with $l = 2$ as a function of the age and the effective temperature for a model of KIC 4351319 computed with a mass $M = 1.32\,M_\odot$ and $Z = 0.03$. Here solid lines correspond to modes with even radial order, and grey dotted lines correspond to modes with odd radial order. The frequency and effective temperature ranges correspond to the observed ones. The vertical line indicates Model 1 of Table 4.

The behaviour of the mixed modes inside the star can be understood by considering the propagation diagram in Fig. 10 obtained for three models of KIC 4351319, calculated, respectively, without extra mixing effect and with the inclusion of a weak and an efficient turbulent diffusion below the convective envelope. The characteristics of the non-radial modes depend on the separation between gravity and acoustic domains, defined, respectively, by the Brunt–Väisälä (N) and Lamb frequencies (S_l). The Lamb frequencies appear close to the g-mode region. Thus, the gravity waves, trapped in a region not so well separated from the region of propagation of the acoustic waves, can interact with the p modes of similar frequencies. In addition, it is possible to notice that at nearly the same value of effective temperature and luminosity, the model without extra-mixing effect shows a second maximum in its buoyancy frequency located at the base of the convective envelope ($r = 0.23R$). This maximum becomes smaller and totally disappears as the effect of the helium diffusion beneath the base of the convective envelope becomes stronger. The characteristics of this second maximum in N reflect the behaviour of the hydrogen abundance inside the star as can be seen in Fig. 7 and it will be discussed in Section 5.4.

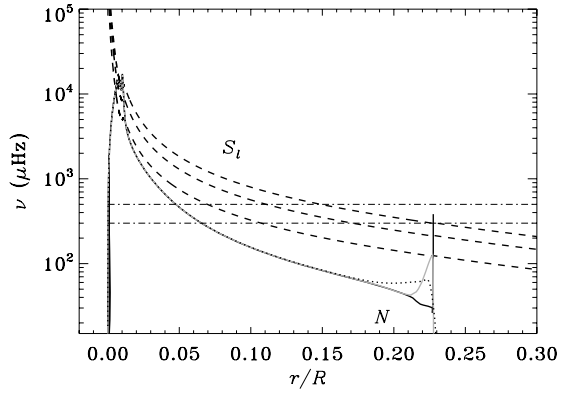

Figure 10. Propagation diagram from the centre to $r = 0.3\,R$ for three models. The solid black line represents the buoyancy frequency N for Model 1 in Table 4 without extra-mixing effects, the solid grey line represents the buoyancy frequency N for Model 2 in Table 4 with the addition of a weak diffusion from the convective envelope, the dotted line represents the buoyancy frequency N for Model 3 in Table 4 with an efficient turbulent diffusion from the convective envelope. The dashed lines represent the Lamb frequencies S_l for $l = 1$, 2, 3. The dot–dashed horizontal lines define the limits of the range of the observed frequencies.

It is important to note that, according to the theory, the spectra of g modes are denser than that of p modes: many g modes can interact with the same p mode of close frequency.

In order to have an idea about the modes expected to be visible, amplitudes of all the calculated modes were roughly estimated by making the following considerations. The total energy of a mode of radial order n and harmonic degree l can be expressed as $\mathcal{E}_{nl} = A_{nl}^2 E_{nl}$, where A_{nl} is the surface amplitude, and E_{nl} is the inertia of the mode. For stochastically excited modes, it is generally expected that the mode energy is independent of the harmonic degree at fixed frequency. It follows that the amplitude of a mode can be estimated relative to a radial mode of the same frequency, such that the modes would have the same total energy (e.g. Christensen-Dalsgaard, Bedding & Kjeldsen 1995; Dupret et al. 2009):

$$\frac{A_{nl}}{A_0} = \left[\frac{E_0}{E_{nl}}\right]^{1/2}, \qquad (6)$$

where A_0 and E_0 have been obtained by interpolating to the frequencies of radial modes. Fig. 11 shows the normalized inertia for the frequencies of Model 1 of Table 4 of KIC 4351319. It shows that radial modes have a very low inertia relative to most of the non-radial modes and are the modes which will show highest amplitude at the surface. Some modes with $l = 1$, $l = 2$ and $l = 3$ have an inertia similar to that of the radial modes $E_{nl} \simeq E_0$, and appear quite regularly spaced in frequency. These modes which preserve strong p-mode character are solar-like oscillations and are predicted to be visible at the surface with a quite high amplitude.

The effect of coupling, typically expected only for $l = 1$, strongly appears also for modes with $l \geq 2$. As the inertia grows, during the coupling the gravity character of the modes predominates on the acoustic character. Modes with the highest inertia are evanescent towards the surface and hence have the lowest probability to be observed. Thus, due to the low amplitude, the probability to detect any mixed modes for $l = 3$ appears quite low, but it is quite likely that we can observe many of the mixed modes for $l = 1$ and probably a few of the mixed modes for $l = 2$ (Beck et al. 2011).

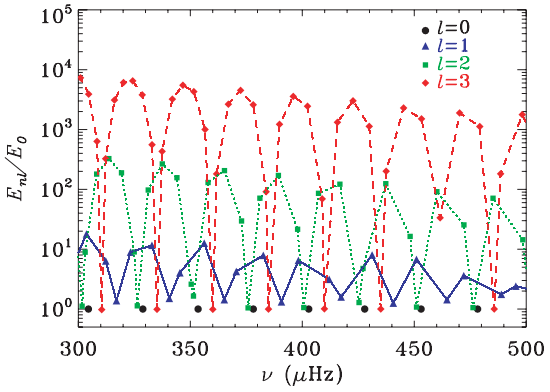

Figure 11. Normalized inertia plotted against frequency for Model 1 described in Table 4. Black circles are employed for $l = 0$ modes. Blue triangles connected by solid lines are employed for $l = 1$ modes. Green squares connected by dotted lines are employed for $l = 2$ modes. Red diamonds connected by dashed lines indicate $l = 3$ modes.

Table 4. Relevant parameters, the mass M, the age, the luminosity L, the effective temperature $T_{\rm eff}$, the initial hydrogen abundance X_0, the surface metallicity $Z_{\rm s}$, the surface radius R, the location $r_{\rm cb}$ of the base of the convective envelope in units of R, the mixing-length parameter α, the diffusion coefficient $D_{\rm max}$ and the overshooting parameter $\alpha_{\rm ov}$ for a set of models of KIC 4351319.

	$M/{\rm M}_\odot$	X_0	$Z_{\rm s}$	Age (Gyr)	$L/{\rm L}_\odot$	$T_{\rm eff}$ (K)	$R/{\rm R}_\odot$	$\log g$	$r_{\rm cb}/R$	α	$D_{\rm max}$ (cm^2 s^{-1})	$\alpha_{\rm ov}$
1	1.32	0.7	0.03	5.29	5.25	4752	3.39	3.50	0.23	1.8	No	No
2	1.32	0.7	0.03	5.28	5.23	4747	3.39	3.50	0.23	1.8	9000	No
3	1.32	0.7	0.03	5.28	5.22	4748	3.38	3.50	0.23	1.8	40 000	No
4	1.32	0.7	0.03	5.27	5.28	4761	3.38	3.50	0.23	1.8	No	0.2
5	1.28	0.7	0.03	5.94	5.06	4734	3.35	3.49	0.22	1.8	80 000	No

In order to clearly distinguish the nature of the mixed modes, it is useful to study the behaviour of the displacement eigenfunctions of the modes. Fig. 12 shows the radial variation of the eigenfunctions of three mixed modes calculated for Model 1 of KIC 4351319 described in Table 4. The upper panels of Fig. 12 show the eigenfunction for a mixed mode with high inertia and hence with a predominant gravity nature, characterized by a quite large amplitude in the core. The middle panels of Fig. 12 show the eigenfunction for a mixed mode with both gravity and pressure character. The lower panels of Fig. 12 show the eigenfunction for a nearly pure acoustic mode, with an inertia comparable to that of the radial modes: the amplitude in the core is negligible.

5.3 Interpretation of the observed oscillation spectrum

Among all the possible models, we selected a few models able to reproduce the set of all the observed frequencies of Table 3 and the observed values of the large and small separations. The characteristics of some models that satisfy the observed constraints are given in Table 4. According to the stellar evolution constraints, given the match with the observed oscillation properties, and with the use of all the possible values of mass and metallicity, our computations show that the age of KIC 4351319 is (5.6 ± 0.4) Gyr, with a mass $M = 1.30 \pm 0.03\,{\rm M}_\odot$, a radius $R = 3.37 \pm 0.03\,{\rm R}_\odot$ and a luminosity $L = 5.1 \pm 0.2\,{\rm L}_\odot$.

The values of mass and radius which have been obtained by direct modelling of the individual frequencies are better constrained and well compatible with those obtained by the scaling laws as described in Section 4.2.

A detailed comparison between the theoretical oscillation spectra for Model 1 and Model 5 of KIC 4351319 reported in Table 4 and the observed data is provided in the échelle diagrams of Fig. 13. The size of the symbols is proportional to the theoretical oscillation amplitudes of p modes, relative to the amplitudes of radial modes with the same frequency (see equation 6). The results show, as explained in previous sections, that the observed modes are $l = 0$ pure acoustic modes, and $l = 1$ and $l = 2$ nearly pure p modes and

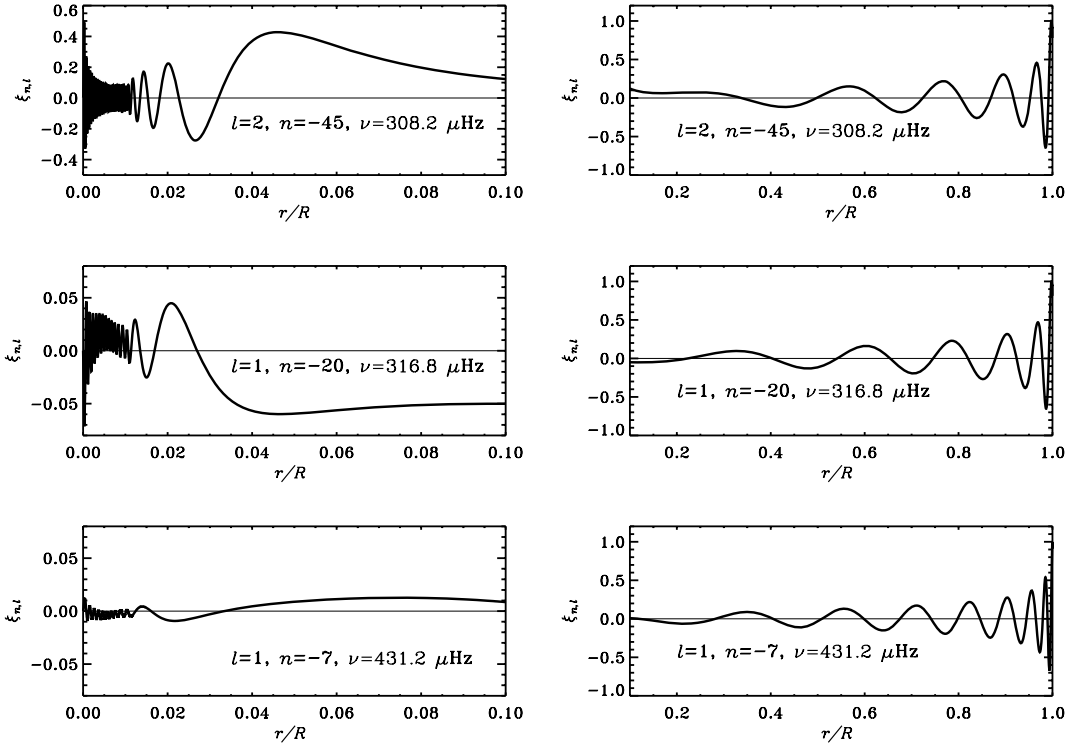

Figure 12. Radial variations of eigenfunctions $\xi_{n,l} = r^{3/2}\rho^{1/2}\,\delta r$ for three selected mixed modes calculated for Model 1 in Table 4. The left panels show the behaviour of the eigenfunction from the centre to $0.1\,R$. The right panels show the eigenfunctions from $0.1\,R$ to the surface. The harmonic degree l, the radial order n and the frequency ν of the modes considered are indicated inside each panel.

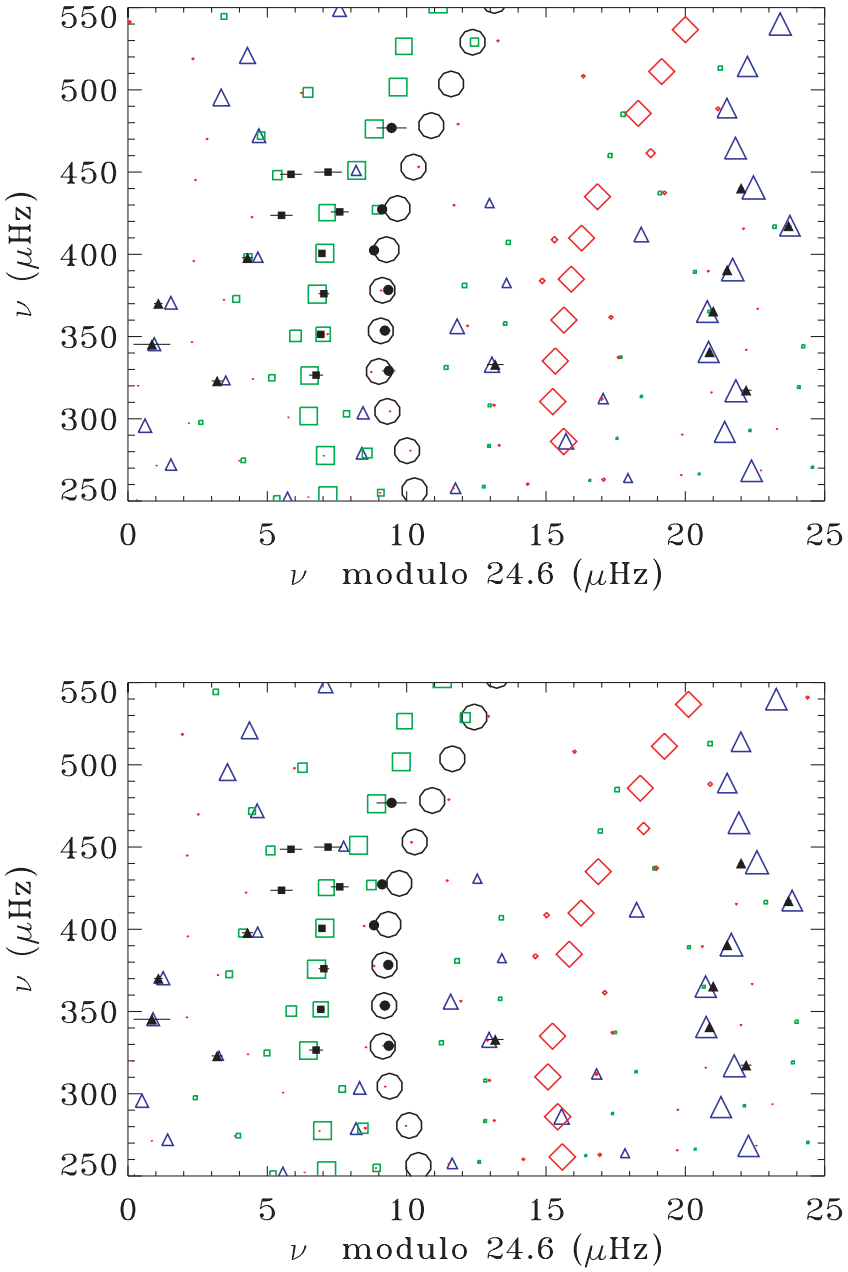

Figure 13. Two échelle diagrams based on observed and computed frequencies, plotted with $\Delta\nu = 24.6$ μHz. The upper panel shows results for Model 1 in Table 4, while the lower panel shows results for Model 5 in Table 4. The open symbols represent computed frequencies, while the filled symbols represent the observed frequencies of Table 3. Circles are used for modes with $l = 0$, triangles for $l = 1$, squares for $l = 2$ and diamonds for $l = 3$. The size of the open symbols indicates the relative surface amplitude of oscillation of the modes.

some $l = 1$ and $l = 2$ g–p mixed modes. Some non-radial modes with mixed gravity-pressure character have an inertia so low as to propagate up to the surface and appear to behave like solar-like oscillations. Very few mixed modes, with a quite high inertia, keep their gravity character, although the combination with a p mode enhance their amplitude so that they can be observed at the surface and in the échelle diagram appear to depart strongly from the regular solar-like pattern.

Pure g modes at lower frequencies have not been detected with the present observations. Solar-like oscillations with $l = 3$, although theoretically predicted, have not been detected, probably due to geometrical reasons which produce the cancellation of the observed signal.

We found that there is a very good agreement between observed and theoretical frequencies. In particular we are able to reproduce all the $l = 1$ mixed modes. The presence of mixed modes with $l = 2$ needs to be better investigated: unfortunately none of our best models, shown in Fig. 13, is able to reproduce the $l = 2$ mode with frequency $\nu = 423.71$ μHz. In addition, the results show that it is quite difficult to determine which of Model 1 and Model 5 best reproduces the observations. Perhaps the ambiguity will be solved by the identification of modes at lower frequencies and in particular if the reality of the mode of 302.32 μHz (see Section 4) will be confirmed or not.

Another important issue is related to the possibility of observing rotational splittings in this star. We estimate that the observed

rotational velocity $v \sin i \simeq 6\,\mathrm{km\,s^{-1}}$, quite high for this kind of objects, might produce a rotational splitting of ∼0.8 μHz for the modes of $l = 2$, $m = \pm 2$ in case of rigid rotation. Such a rotational splitting is about twice the value of the frequency resolution of the 30 *d* data set. To check for the signature of rotation we have re-run the frequency determination now adding rotational split components for $l = 1$ and $l = 2$ modes. The rotation frequency and the inclination angle were allowed to vary in the range between 0 and 3 μHz and 0° and 90°, respectively, following the approach of Gizon & Solanki (2003). A comparison of the global likelihoods of the two models (with and without rotation) indicates that the rotation-free model is about 70 times more likely than the model including rotation.

Indeed, the presence of two modes closely spaced in frequency does not prove that we deal with rotational splitting although this possibility cannot be excluded. Moreover, the two pairs of close frequencies of $l = 2$ suspected for evidence of rotational splittings (448.65 μHz with 449.98 μHz and 423.71 μHz with 425.80 μHz) appear to be not separated by a same amount in frequency, indicating that they cannot be both appearance of rotational splittings.

We finally notice that in order to reproduce the observed modes, we did not correct the frequencies for the surface effects, as suggested by Kjeldsen, Bedding & Christensen-Dalsgaard (2008b), but the small departure of the $l = 0$ modes at high frequency might be indicative of the need of such a correction. In fact, the structure of the near-surface regions of the stars is quite uncertain: there are still substantial ambiguities in modelling the convective flux, defining an appropriate equation of state to describe the thermodynamic properties of the stellar structure, as well as in the treatment of non-adiabatic effects. The conditions and limits of the applicability of the surface effect are still unknown and will be the subject of future studies.

Since there is no evidence for fast rotation, we exclude any possible effect on the frequencies due to magnetic activity.

It was possible to determine the evolutionary state of this star through direct modelling, which places it in the hydrogen-shell-burning phase at the base of the ascending red-giant branch. This star is substantially less evolved than the red giants whose $l = 1$ gravity-mode period spacings were measured by Bedding et al. (2011) and Mosser et al. (2011b). This is reflected in Fig. 8 where we see that the spacing of the g-dominated modes (the upward sloping features) is comparable to the p-mode spacing. This fact, together with the very strong mode bumping, makes it quite hard to see a regular spacing in the $l = 1$ modes of any single model. This makes it difficult to measure a clear g-mode period spacing. However, we see from the list of observed modes in Table 3 that the consecutive $l = 1$ modes have period spacings in the range 35–50 s, which is consistent with a hydrogen-shell-burning star (Bedding et al. 2011). Applying the method described by Mosser et al. (2011b) confirms a period spacing of about 40 ± 4 s.

5.4 Sharp features inside KIC 4351319

Fig. 14 shows that a weak oscillatory motion is present in the calculated frequencies for the acoustic modes which follow closely the asymptotic law, namely the radial modes and the non-radial modes with very low inertia. This oscillatory signal, as explained in Section 3.3, is produced only by the region of the second ionization of helium, which induces a local minimum in the first adiabatic coefficient Γ_1 and hence a sharp variation in the sound speed.

Fig. 15, which shows the behaviour of the first adiabatic coefficient as a function of the acoustic radius $t = \int_0^{r_1} \mathrm{d}r/c(r)$, indicates that in the models of KIC 4351319 the second helium ionization

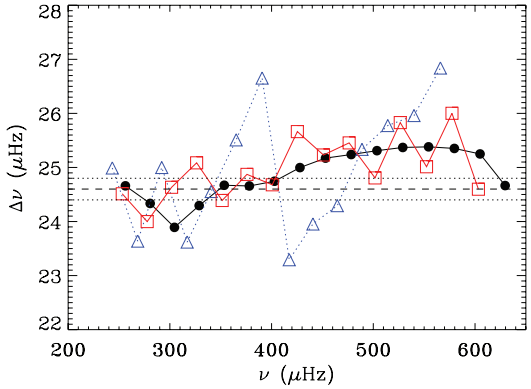

Figure 14. Small oscillations in the large frequency separation for acoustic modes of $l = 0$ (black dots), $l = 1$ (blue triangles) and $l = 2$ (red squares) as calculated for Model 1 of Table 4. Observed large separation and its errors $\Delta\nu = 24.6 \pm 0.2$ μHz are indicated by dashed and dotted lines, respectively.

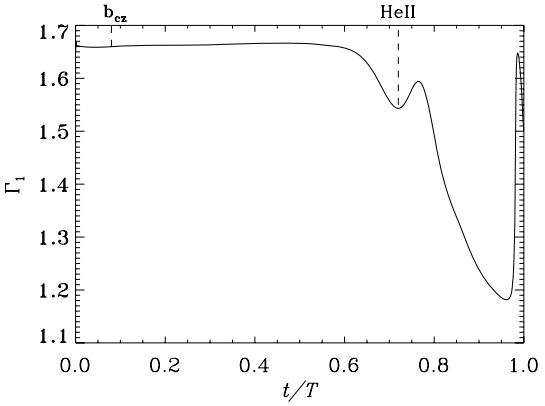

Figure 15. First adiabatic exponent as a function of the acoustic radius, in units of the surface value *T*, for Model 1 of Table 4. The region where helium undergoes its second ionization corresponds to the second minimum in Γ_1. The location of the base of the convective envelope is also indicated.

zone occurs at about $t_{\mathrm{He\,II}}/T \simeq 0.7$, while the base of the convective envelope is located at $t_{\mathrm{b_{cz}}}/T \simeq 0.08$, too deeply to produce an effective signal into the solar-like frequencies (Miglio et al. 2010). The properties of the helium ionization zone, once determined from the oscillation frequencies, may be used to constrain the structure of the star, in particular the envelope helium abundance. Further studies and developments are required in order to determine how a different content of He and a different equation of state for the computation of the models will result in a different oscillatory behaviour in the theoretical frequencies.

Secondly, we have also considered the possibility to isolate the signal coming from the base of the convective envelope by looking at the observed modes which penetrate deeply inside the star, namely the mixed modes with a high inertia. This can be studied following Miglio et al. (2008), by comparing models modified by adding turbulent diffusion or overshooting at the base of the convective envelope. The results have shown that the inclusion of turbulent diffusion, or overshooting, below the convective envelope produces a displacement only in the mixed modes for $l = 1$ and $l = 2$ modes, while all the other frequencies are not modified as shown in Fig. 16. Thus, although we have not observed high-order g modes, we can still use the mixed modes to probe qualitatively the interior of this star. However, it is impossible to distinguish the

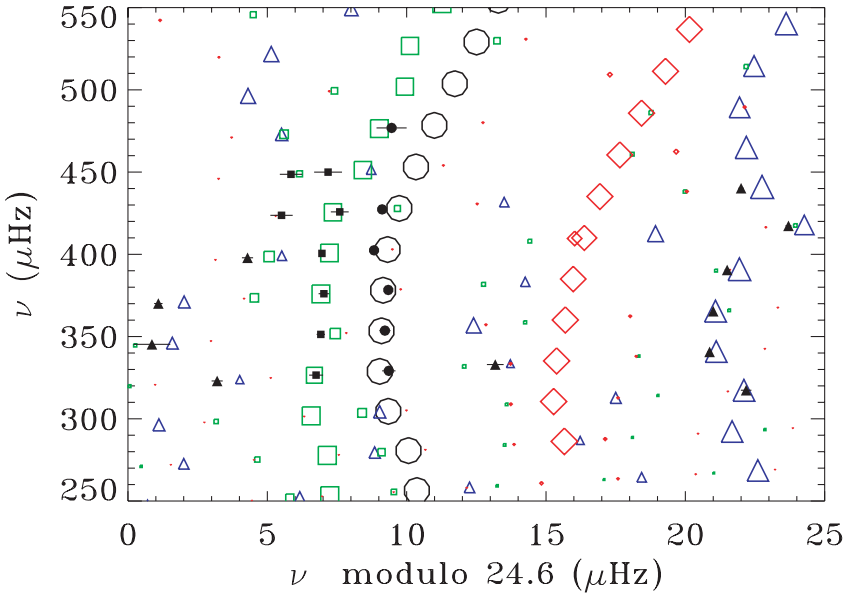

Figure 16. Échelle diagram based on observed and computed frequencies plotted with $\Delta\nu = 24.6\,\mu$Hz. The open symbols show computed frequencies for Model 2 calculated with turbulent diffusion and described in Table 4. Circles are used for modes with $l = 0$, triangles for $l = 1$, squares for $l = 2$, diamonds for $l = 3$. The size of the open symbols indicates the relative surface amplitude of oscillation of the modes.

effect on the frequencies due to the inclusion of diffusion from that of overshooting.

6 CONCLUSION

KIC 4351319 has been observed for 30 d by the *Kepler* satellite. These observations have yielded a clear detection of 25 modes identified with harmonic degrees $l = 0$, 1, 2 between 300 and 500 μHz with a large separation $\Delta\nu_0 = 24.6 \pm 0.2$ μHz and a small separation $\delta\nu_{02} = 2.2 \pm 0.3$ μHz, respectively.

The oscillation spectrum of this star is characterized by the presence of a well-defined solar-like oscillations pattern due to radial acoustic modes and non-radial nearly pure p modes equally spaced in frequencies. The nearly pure p modes have mixed gravity-pressure character with an inertia so low as to propagate up to the surface and appear to behave like solar-like oscillations, although they penetrate deeply to the core.

The oscillation spectrum also showed evidence for the presence of mixed modes with strong gravity-mode character. Those modes sound the internal region of this star and, besides constraining the stellar age, carry tight information about the location of the convective envelope and the condition in the core. This enabled to define characteristics of this star with an accuracy which cannot be reached by the use of only the global asteroseismic parameters, $\Delta\nu$ and $\nu_{\rm max}$.

Thus, in this paper we have addressed the problem of identifying the structural properties and the evolutionary state of KIC 4351319 by using the results of the analysis of the oscillation spectrum and the atmospheric parameters provided by supplementary ground-based spectroscopic observations.

Detailed modelling of this star, in an attempt to match both the asteroseismic and spectroscopic constraints, allowed us to determine the main parameters with an unprecedented level of precision for a red-giant star, with uncertainties of 2 per cent for mass, 7 per cent for age, 1 per cent for radius and 4 per cent for luminosity. In the end, we are able to conclude that this star is in the red-giant phase of the evolution, with a mass $M = (1.30 \pm 0.03)\,M_\odot$, an age of 5.6 ± 0.4 Gyr, a radius $R = 3.37 \pm 0.03\,R_\odot$ and a luminosity $L = 5.1 \pm 0.2\,L_\odot$. The uncertainties obtained for the stellar parameters come from the degeneracy of the models describing the stars in the red-giant phase of the evolution.

Only the detection of g modes, which better sound the condition of the core, could improve the results obtained by the present analyses, while strong theoretical efforts need to be done in order to achieve a better description of the stellar structure.

It is clear that KIC 4351319 represents an excellent candidate for long-term observations, which have been already scheduled for *Kepler* future runs. This will allow us to open a window on the understanding of this phase of the evolution and to unveil all the raised questions including those relative to the identification of the mixed modes, to the signature of the ionization of the He and to the presence of diffusion or overshooting below the convective envelope. In particular, the possibility to detect rotational splittings in KIC 4351319 appears very fascinating and represents an excellent opportunity for sounding the internal dynamics of a red-giant star.

ACKNOWLEDGMENTS

Funding for this mission is provided by NASA's Science Mission Directorate. We thank the entire *Kepler* team for the development and operations of this outstanding mission.

The work presented here is also based on observations obtained with the Harlan J. Smith Telescope at McDonald Observatory, Texas.

SH acknowledges financial support from the UK Science and Technology Facilities Council (STFC). SH acknowledges financial support from the Netherlands Organization for Scientific Research (NWO).

KU acknowledges financial support by the Deutsche Forschungsgemeinschaft (DFG) in the framework of project UY 52/1-1.

TK is supported by the Canadian Space Agency and the Austrian Science Fund (FWF P22691-N16).

REFERENCES

Aigrain S., Favata F., Gilmore G., 2004, A&A, 414, 1139
Aizenman M., Smeyers P., Weigert A., 1977, A&A, 58, 41
Allende Prieto C., Barkelm P. S., Lambert D. L., Cunha K., 2004, A&A, 420, 183
Anderson E. R., Duvall T. L., Jr, Jefferies S. M., 1990, ApJ, 364, 699
Angulo C. et al., 1999, Nucl. Phys. A, 656, 3
Asplund M., Grevesse N., Sauval A. J., Scott P., 2009, ARA&A, 47, 481
Ballot J., Turck-Chièze S., and García R. A., 2004, A&A, 423, 1051
Barban C. et al., 2007, A&A, 468, 1033
Basu S., Mazumdar A., Antia H. M., Demarque P., 2004, MNRAS, 350, 277
Beck P. et al., 2011, Sci, 332, 205
Bedding T. R., Kjeldsen H., 2003, Publ. Astron. Soc. Austr., 20, 203
Bedding T. R. et al., 2005, A&A, 432, L43
Bedding T. R. et al., 2010, ApJ, 713, L176
Bedding T. R. et al., 2011, Nat, 471, 608
Biazzo K., Frasca A., Catalano S., Marilli E., 2007, Astron. Nachr., 328, 938
Böhm-Vitense E., 1958, Zeitschrift für Astrophysik, 46, 1115
Borucki W. J. et al., 2010, Sci, 327, 977
Buzasi D., Catanzarite J., Laher R., Conrow T., Shupe D., Gautier T. N., III, Kreidl T., Everett D., 2000, ApJ, 532, L133
Chaplin W. J., Elsworth Y., Isaak G. R., Marchenkov K. I., Miller B. A., New R., Pinter B., Appourchaux T., 2002, MNRAS, 336, 979
Christensen-Dalsgaard J., 1988, in Christensen-Dalsgaard J., Frandsen S., eds, Proc. IAU Symp. 123, Advances in Helio- and Asteroseismology. Kluwer, Dordrecht, p. 295
Christensen-Dalsgaard J., 2004, Sol. Phys., 220, 137
Christensen-Dalsgaard J., 2008a, Ap&SS, 316, 13
Christensen-Dalsgaard J., 2008b, Ap&SS, 316, 113
Christensen-Dalsgaard J., Proffitt C. R., Thompson M. J., 1993, ApJ, 403, 75
Christensen-Dalsgaard J., Bedding T. R., Kjeldsen H., 1995, ApJ, 443, L29
De Ridder J. et al., 2009, Nat, 459, 398
Di Mauro M. P., Christensen-Dalsgaard J., Kjeldsen H., Bedding T. R., Paternò L., 2003, A&A, 404, 341
Dupret M. A. et al., 2009, A&A, 506, 57
Dziembowski W. A., Gough D. O., Houdek G., Sienkiewicz R., 2001, MNRAS, 328, 601
ESA, 1997, The Hipparcos and Tycho Catalogues, ESA SP-1200. ESA Publications Division, Noordwijk
Frandsen S. et al., 2002, A&A, 394, L5
García R. A. et al., 2009, A&A, 506, 41
García R. A. et al., 2011, MNRAS, 414, L6
Gilliland R. L. et al., 2010, PASP, 122, 131
Gizon L., Solanki S. K., 2003, ApJ, 589, 1009
Grevesse N., Noels A., 1993, in Prantzos N., Vangioni-Flam E., Cassé M., eds, Origin and Evolution of the Elements. Cambridge Univ. Press, Cambridge, p. 15
Grey R., 1992, The Observation and Analysis of Stellar Photospheres. Cambridge Univ. Press, Cambridge
Grubebauer M., Kallinger T., Weiss W. W., Guenther D. B., 2009, A&A, 506, 1043
Guenther D. B., Demarque P., Buzasi D., 2000, ApJ, 530, L45
Harvey, J., 1985, in Rolfe E., Battrick B., eds, ESA SP-576, Proceedings Future Missions in Solar, Heliospheric and Space Plasma Physics. ESA Publications Division, Noordwijk, p. 199
Hekker S. et al., 2009, A&A, 506, 465
Hekker S., Barban C., Baudin F., De Ridder J., Kallinger T., Morel T., Chaplin W. J., Elsworth Y., 2010a, A&A, 520, 60
Hekker S. et al., 2010b, ApJ, 713, L187
Houdek G., Gough D. O., 2007, MNRAS, 375, 861
Huber D., Stello D., Bedding T. R., Chaplin W. J., Arentoft T., Quirion P.-O., Kjeldsen H., 2009, Commun. Asteroseismol., 160, 74
Huber D. et al., 2010, ApJ, 723, 1607
Iglesias C. A., Rogers F. J., 1996, ApJ, 464, 943
Jenkins J. M. et al., 2010, ApJ, 713, L87
Kallinger T., et al.2008a, Commun. Asteroseismol., 153, 84
Kallinger T. et al., 2008b, A&A, 478, 497
Kallinger T. et al., 2010a, A&A, 509, 77
Kallinger T. et al., 2010b, A&A, 522, 1
Kjeldsen H., Bedding T., 1995, A&A, 293, 87
Kjeldsen H., Bedding T. R., Viskum M., Frandsen S., 1995, AJ, 109, 1313
Kjeldsen H. et al., 2008a, ApJ, 682, 1370
Kjeldsen H., Bedding T. R., Christensen-Dalsgaard J., 2008b, ApJ, 683, L175
Koch D. G. et al., 2010, ApJ, 713, 79
Kurucz R. L., 1993, in Dworetsky M. M., Castelli F., Faraggiana R., eds, ASP Conf. Ser. Vol. 44, A New Opacity-sampling Model Atmosphere Program for Arbitrary Abundances. Peculiar versus Normal Phenomena in A-type and Related Stars. IAU Colloquium 138, Astron. Soc. Pac., San Francisco, p. 87
Kurucz R. L., Avrett E. H., 1981, SAO Special Rep. 391
Lampton M., Margon B., Bowyer S., 1976, ApJ, 208, 177
Latham D. W., Brown T. M., Monet D. G., Everett M., Esquerdo G. A., Hergenrother C. W., 2005, BAAS, 37, 1340
Lenz P., Breger M., 2005, Commun. Asteroseismol., 146, 53
Lopes I., Turck-Chieze S., Michel E., Goupil M.-J., 1997, ApJ, 480, 794
Mathur S. et al., 2010, A&A, 518, 53
Mazumdar A., Antia H. M., 2001, A&A, 377, 192
Merline W. J., 1999, in Hearnshaw J. B., Scarfe C. D., eds, ASP Conf. Ser. Vol. 185, Precise Stellar Radial Velocities. Astron. Soc. Pac., San Francisco, p. 187
Metcalfe T. S. et al., 2010, ApJ, 723, 1583
Miglio A., Christensen-Dalsgaard J., Di Mauro M. P., Monteiro M. J. P. F. G., Thompson M. J., 2003, in Thompson M. J., Cunha M. S., Monteiro M. J. P. F. G., eds, Asteroseismology Across the HR Diagram. Kluwer, Dordrecht, p. 537
Miglio A., Montalbán J., Noels A., Eggenberger A., 2008, MNRAS, 386, 1487
Miglio A. et al., 2009, A&A, 503, L21
Miglio A. et al., 2010, A&A, 520, L6
Milne A. A., 1926, Winnie-the-Pooh. Methuen & Co. Ltd, London
Montalbán J., Miglio A., Noels A., Scuflaire R., Ventura P., 2010, ApJ, 721, L182
Monteiro M. J. P. F. G., Thompson M. J., 1998, in Deubner F.-L., Christensen-Dalsgaard J., Kurtz D. W., eds, New Eyes to See Inside the Sun and Stars, Proc. IAU Symp. 185, Kluwer, Dordrecht, p. 317
Monteiro M. J. P. F. G., Christensen-Dalsgaard J., Thompson M. J., 2000, MNRAS, 316, 165
Mosser B., Appourchaux T., 2009, A&A, 508, 877
Mosser B. et al., 2010, A&A, 517, 22
Mosser B. et al., 2011a, A&A, 525, 9
Mosser B. et al., 2011b, A&A, in press
Pallè P. L., Roca Cortés T., Jiménez A., GOLF Team, VIRGO Team, 1999, in Gimenez A., Guinan E. F., Montesinos B., eds, ASP Conf. Ser. Vol. 173, Stellar Structure Theory and Convective Energy Transport. Astron. Soc. Pac., San Francisco, p. 297
Pérez Hernández F., Christensen-Dalsgaard J., 1998, MNRAS, 295, 344
Proffitt C. R., Michaud G. J., 1991, ApJ, 380, 238
Retter A., Bedding T. R., Buzasi D. L., Kjeldsen H., Kiss L. L., 2003, ApJ, 591, L151
Retter A., Bedding T. R., Buzasi D. L., Kjeldsen H., Kiss L. L., 2004, ApJ, 601, L95
Rogers F. J., Nayvonov A., 2002, ApJ, 576, 1064
Stello D., Kjeldsen H., Bedding T. R., De Ridder J., Aerts C., Carrier F., Frandsen S., 2004, Sol. Phys., 220, 207
Tassoul M., 1980, ApJS, 43, 469
Teixeira T. et al., 2003, Ap&SS, 284, 233
Uytterhoeven K. et al., 2010a, Astron. Nachr., 331, 993
Uytterhoeven K. et al., 2010b, Astron. Nachr., in press

APPENDIX A: MAXIMUM LIKELIHOOD ESTIMATORS

According to this method, the p-mode parameters are estimated by finding the best fit between a modelled and the observational power density spectrum by using a maximum-likelihood technique (Anderson et al. 1990). Two different models have been assumed.

A1 Lorentzian with convolution of the window function

The fitting of the non-oversampled power spectrum has been done in two steps. First the background, for which we use a power-law fit to account for long-term effects, such as granulation, rotation or activity related to spots, is fitted. Then, we computed a global maximum-likelihood fit (Anderson et al. 1990) to all oscillation modes, where the final model M is a convolution of the model with the power spectrum of the observed window function of the data set, normalized to unit total area (see equation A1). This takes the redistribution of power caused by gaps in the data into account.

$$M = \left(\sum_j \frac{H_j}{1 + ((\nu_{\mathrm{cen},j} - \nu)/B_j)^2} \right) * \text{window}. \tag{A1}$$

In this model the previously determined background is kept fixed, while each of the jth oscillation peak is fitted with the height (H), the central frequency (ν_{cen}) and HWHM (B) and the noise level as free parameters.

The selection of the oscillation modes is based on a statistical test of the binned power spectrum. For this test we bin the power spectrum over intervals of three frequency bins. Then we compute the probability of the power in the binned power spectrum to be due to noise. This probability is computed using a χ^2 distribution in which we take the width and number of the bins into account in the degrees of freedom. Frequencies at which the probability of the power not being due to white noise is larger than 95 per cent are selected as candidate oscillation frequencies. After performing the fit, we also verify that in the ratio of the observed to the fitted spectra no prominent peaks are left. Therefore, we compute the relative height for the investigated frequency range for which the probability of observing at least one spike with this height due to noise is 10 per cent, following the formulation by Chaplin et al. (2002) and references therein.

This is also described in Hekker et al. (2010a).

A2 Sum of Lorentzians or sinc

If the modes are resolved (i.e. the mode width is larger than the frequency resolution) we chose to model the oscillation spectrum by a sum of Lorentzians plus a background model that accounts for the signal which is not due to the p modes such as the instrumental noise or stellar background. In the frequency range considered here, the background has been modelled by a straight line (i.e. $a + b\nu$). When the mode width is of the order of the frequency resolution we change the sum of Lorentzians to a sum of sinc.

The modelled power spectrum used to match the data is

$$P(\nu_k) = \sum_{n=1}^{Q} \mathcal{M}(n, \nu_k) + B(\nu_k), \tag{A2}$$

where Q is the number of oscillation modes, n labels the modes, ν_k is the Fourier frequency and $B(\nu_k)$ the background noise in the power spectrum, modelled as a straight line, i.e. $a + b\nu_k$ with a and b two constants and free parameters of the fit. $\mathcal{M}(n, \nu_k)$ is a Lorentzian when the mode width is larger than the frequency resolution:

$$\mathcal{M}(n, \nu_k) = H_n \frac{1}{1 + \left(\frac{2(\nu_k - \nu_n)}{\Gamma_n} \right)^2}, \tag{A3}$$

where H_n is the height of the Lorentzian profile, ν_n is the oscillation mode frequency and Γ is the mode line width (FWHM) with $\Gamma = 1/(\pi\tau)$, τ being the mode lifetime.

When the modes are not resolved, $\mathcal{M}(n, \nu_k)$ is a sinc function:

$$\mathcal{M}(n, \nu_k) = H_n \mathrm{sinc}^2(\pi T(\nu_k - \nu_n)) \tag{A4}$$

where T is the total length of the observing run.

The power spectrum is fitted 'globally' over a frequency range corresponding to the detected excess power. The free parameters of the fitting process are as follows.

(i) The height of the Lorentzian profile, H_n, n being the radial order. A single height parameter is fitted per mode.
(ii) The frequency for each mode, ν_n.
(iii) The line width for each mode (FWHM) with $\Gamma_n = 1/(\pi\tau_n)$, τ_n being the mode lifetime. A single width has been considered.
(iv) The parameters a, b describing the background model as mentioned above.

The mode-parameter 1σ error bars are derived from the Hessian matrix. No oversampling has been used in the computation of the power spectrum for the fitting procedure in order to minimize the correlation of the points. The degree of each mode is identified using échelle diagrams.

APPENDIX B: BAYESIAN MCMC METHOD

The p-mode parameters are estimated by fitting a sequence of Lorentzian profiles to the power density spectrum, where we use the previously determined stellar activity and granulation signal (equation 4 without the Gaussian) as a fixed background. The visually identified mode profiles are parametrized by their central frequencies, mode heights and lifetimes. As can be seen in Fig. 2, the mode profiles are quite narrow. To prevent the algorithm from overfitting the data and to keep the number of free parameters to a reasonable amount we use two lifetime parameters, one for $l = 0$ and 2 modes and one for $l = 1$ modes. Furthermore, we assume the individual mode heights to follow a Gaussian envelope parametrized by a single central frequency and width but with individual heights for each mode degree. For the 25 modes in Table 3, this results in a total of 32 free parameters. For the fit we use a Bayesian MCMC algorithm (Gruberbauer et al. 2009) that delivers probability density functions for all fitted parameters and their marginal distributions, from which we compute the most probable values and their 1σ uncertainties. During the fit the mode frequency parameters are allowed to vary independently within ± 2 μHz around the value inferred from a visual inspection of the spectrum. The lifetimes are kept between 1 and 50 d. Whereas the centre and width of the Gaussian envelope are kept within 0.9 and 1.1 times ν_{max} and σ (equation 4), respectively, the height for each mode degree is allowed to vary independently between 0 and 2 times the highest peak in power density spectrum.

This paper has been typeset from a TEX/LATEX file prepared by the author.